10178–10191 *Nucleic Acids Research, 2021, Vol. 49, No. 17* *Published online 25 August 2021*
https://doi.org/10.1093/nar/gkab738

Insights into the dual functions of AcrIF14 during the inhibition of type I-F CRISPR–Cas surveillance complex

Xi Liu[1,†], Laixing Zhang[2,†], Yu Xiu[1,†], Teng Gao[1,†], Ling Huang[1], Yongchao Xie[1], Lingguang Yang[1], Wenhe Wang[2], Peiyi Wang[3,*], Yi Zhang[1,*], Maojun Yang[2,*] and Yue Feng[1,*]

[1]Beijing Advanced Innovation Center for Soft Matter Science and Engineering, Beijing Key Laboratory of Bioprocess, State Key Laboratory of Chemical Resource Engineering, College of Life Science and Technology, Beijing University of Chemical Technology, 100029 Beijing, China, [2]Ministry of Education Key Laboratory of Protein Science, Beijing Advanced Innovation Center for Structural Biology, Beijing Frontier Research Center for Biological Structure, School of Life Sciences, Tsinghua University, Tsinghua-Peking Center for Life Sciences, 100084 Beijing, China and [3]Cryo-EM Centre, Department of Biology, Southern University of Science and Technology, 515055 Shenzhen, China

Received March 15, 2021; Revised July 20, 2021; Editorial Decision August 11, 2021; Accepted August 17, 2021

ABSTRACT

CRISPR–Cas systems are bacterial adaptive immune systems, and phages counteract these systems using many approaches such as producing anti-CRISPR (Acr) proteins. Here, we report the structures of both AcrIF14 and its complex with the crRNA-guided surveillance (Csy) complex. Our study demonstrates that apart from interacting with the Csy complex to block the hybridization of target DNA to the crRNA, AcrIF14 also endows the Csy complex with the ability to interact with non-sequence-specific dsDNA as AcrIF9 does. Further structural studies of the Csy–AcrIF14–dsDNA complex and biochemical studies uncover that the PAM recognition loop of the Cas8f subunit of the Csy complex and electropositive patches within the N-terminal domain of AcrIF14 are essential for the non-sequence-specific dsDNA binding to the Csy–AcrIF14 complex, which is different from the mechanism of AcrIF9. Our findings highlight the prevalence of Acr-induced non-specific DNA binding and shed light on future studies into the mechanisms of such Acr proteins.

INTRODUCTION

Clustered regularly interspaced short palindromic repeats (CRISPR) and CRISPR-associated (Cas) proteins constitute a delicate adaptive immune system of prokaryotes, to prevent predations by phages and other mobile genetic elements (MGEs) (1). CRISPR–Cas systems are widely distributed among prokaryotes, present in almost all archaea and ∼60% of bacteria (2). CRISPR–Cas systems protect the prokaryotes against MGEs through three stages (adaptation, biogenesis and interference). In the first stage, the foreign nucleic acid segments are incorporated into the CRISPR array as spacers in the genome of the host bacteria. Subsequently, the CRISPR array region is transcribed and matured into CRISPR RNA (crRNA) which contains short repeats and spacers. In the interference stage, Cas proteins associate with crRNA to form ribonucleoprotein complexes which detect and degrade the invasive nucleic acids complementary to crRNA through recognizing the protospacer adjacent motif (PAM) within the foreign nucleic acids and base pairing between the spacer and the target sequence. CRISPR–Cas systems are divided into class I systems, which deploy multi-subunit surveillance complexes guided by crRNA, and class II systems, which utilize crRNA-guided single-subunit multi-domain Cas proteins. The two classes are further divided into six types (types I–VI) and 33 subtypes (44 subtypes including the variants of several subtypes) (3). Class I CRISPR–Cas systems include types I, III, and IV, and are further divided into seven subtypes: I-A through I-F and I-U. The type I-F CRISPR–Cas system of *Pseudomonas aeruginosa* encodes a 350-kDa crRNA-guided surveillance complex (i.e. the Csy complex), comprising four types of Cas pro-

*To whom correspondence should be addressed. Tel: +86 10 6442 1335; Email: fengyue@mail.buct.edu.cn
Correspondence may also be addressed to Yi Zhang. Tel: +86 10 6443 8262; Email: zhangyishirly@hotmail.com
Correspondence may also be addressed to Maojun Yang. Tel: +86 10 6278 9400; Email: maojunyang@tsinghua.edu.cn
Correspondence may also be addressed to Peiyi Wang. Tel: +86 755 8801 8486; Email: wangpy@sustech.edu.cn
†The authors wish it to be known that, in their opinion, the first four authors should be regarded as Joint First Authors.

teins (one Cas5f, one Cas8f, one Cas6f and six Cas7f proteins) and a single 60-nt crRNA (4–7). The Csy complex folds into an asymmetric spiral, in which the Cas6f (formerly Csy4) subunit is stably associated with the 3′ end of the crRNA in the head region. In the tail region, one Cas5f (formerly Csy2) and one Cas8f (formerly Csy1) form a stable heterodimer in which the 5′ handle of the crRNA is anchored. Six Cas7f (formerly Csy3) subunits form the spiral backbone with extensive interactions with the crRNA.

In turn, to effectively bypass the CRISPR–Cas immune systems, phages and other MGEs encode anti-CRISPR (Acr) proteins to inactivate the CRISPR–Cas systems (8–10). Since their first discovery in 2013 (11), a large number of Acrs have been discovered to target type I, II, III, V and VI CRISPR–Cas systems through many different mechanisms. Regarding the stages of CRISPR immunity, Acrs can target the CRISPR–Cas systems during complex assembly, target DNA binding and its cleavage (9). As for the modes of action, most Acrs target the CRISPR–Cas systems through direct and stable binding, while three Acrs so far have been demonstrated to exhibit enzymatic activities (12–14). For Acrs of the type I-F CRISPR–Cas system, AcrIF1-5 were discovered in 2013, which were also the first reported Acrs (11), and then AcrIF6-10 were discovered by bioinformatic approaches (15). In 2018, Bondy-Denomy and colleagues discovered AcrIF11-14 and also a fusion protein AcrIE4-F7 (16). Recently, another 10 type I-F Acr genes were uncovered, ranging from AcrIF15 to AcrIF24, rendering the type I-F Acr family the largest Acr family (17). The structural basis of the mechanism of type I-F Acrs has been determined for AcrIF1 and AcrIF2 (4–6), AcrIF3 (7,18,19), AcrIF6/8/9 (20,21), AcrIF7 (22), AcrIF10 (5) and AcrIF11 (14). A canonical suppression strategy of Acr is sterically blocking the hybridization between the complementary DNA strand and the crRNA. For type I-F Acrs, AcrIF1/2/6/7/8/9/10 all adopt this strategy. Among these Acrs, interestingly, AcrIF9 also exhibits another layer of suppression through inducing non-sequence-specific DNA binding to the Csy complex (21,23).

In this study, we elucidate the mechanism of how AcrIF14 inactivates the type I-F CRISPR system. The biochemical and structural data revealed that AcrIF14 also induces non-sequence-specific DNA binding to the Csy complex apart from engaging the Cas7.4f and Cas7.6f subunits to sterically prevent target DNA binding, reminiscent of AcrIF9. Further mechanistic studies showed that the electropositive patches within the N-terminal domain of AcrIF14 and the PAM recognition loop of the Cas8f subunit of the Csy complex are essential for the non-sequence-specific DNA binding to the Csy–AcrIF14 complex. Comparison between the mechanisms of AcrIF14- and AcrIF9-induced DNA sequestration suggested that they differ in several aspects. In all, our study reports the AcrIF14-induced non-specific DNA binding, illustrates the molecular mechanism of this strategy, and sheds light on future studies into the mechanisms of such Acr proteins.

MATERIALS AND METHODS

Protein expression and purification

The full-length AcrIF14 gene was synthesized by GenScript, amplified by PCR and cloned into pGEX6p-1 to produce a GST-tagged fusion protein with a PreScission Protease cleavage site between GST and the target protein. The AcrIF14 mutants were generated by two-step PCR and were subcloned, overexpressed and purified in the same way as wild-type protein. The full-length AcrIF9 gene was also synthesized by GenScript and cloned into pET28a to produce a His-tagged fusion protein. The GST-tagged and His-tagged proteins were purified as described (14), respectively. Briefly, the proteins were expressed in *Escherichia coli* strain BL21 and induced by 0.2 mM isopropyl-β-D-thiogalactopyranoside (IPTG) when the cell density reached an $OD_{600\,nm}$ of 0.8. For GST-tagged proteins, the cells were harvested, re-suspended in lysis buffer (1× PBS, 2 mM DTT and 1 mM PMSF) and lysed by sonication. The cell lysate was centrifuged and the supernatant was applied onto a self-packaged GST-affinity column (2 ml glutathione Sepharose 4B; GE Healthcare) and contaminant proteins were removed with wash buffer (lysis buffer plus 200 mM NaCl). The fusion protein was then digested with PreScission protease at 4 °C overnight. The protein with an additional five-amino-acid tag (GPLGS) at the N-terminus was eluted with lysis buffer. The eluant was concentrated using an Ultrafree 5000 molecular-weight cutoff filter unit (Millipore) and further purified using a Superdex-200 (GE Healthcare) column equilibrated with a buffer containing 10 mM Tris–HCl pH 8.0, 200 mM NaCl and 5 mM DTT. The fractions containing the target protein were pooled and concentrated to 20 mg/ml. Selenomethionine (Se-Met)-labeled AcrIF14 was expressed in *E. coli* B834 (DE3) cells grown in M9 minimal medium supplemented with 60 mg/l SeMet (Acros) and specific amino acids: Ile, Leu and Val at 50 mg/l; Lys, Phe and Thr at 100 mg/l. The SeMet protein was purified as described above. Recombinant His-tagged protein was purified by Ni-affinity column chromatography and ion exchange chromatography, and was further subjected to gel filtration chromatography (Superdex-200 column) in buffer containing 10 mM Tris–HCl pH 8.0, 200 mM NaCl and 5 mM DTT.

The Cas2/3 gene was cloned into a modified pETDuet-1 vector with a GST tag at the N terminus of the protein and transformed into *E. coli* strain BL21. The protein was purified through GST column, similar as AcrIF14, and then by heparin chromatography and gel filtration. For the *P. aeruginosa* Csy complex including crRNA, the Cas8f/Cas5f, Cas7f/Cas6f and crRNA fragment were cloned into pETDuet-1, pACYCDuet-1 and pRSFDuet-1, respectively. The Csy complex was generated through co-expression of the three plasmids in *E. coli* strain BL21, in which Cas7f is tagged with 6xHis. The mutations of Cas8f were made as above and the Csy complex with Cas8f mutations were purified similarly as the wild-type complex. For the Csy-Acr complexes, Cas8f/Cas5f, Cas7f/Cas6f, crRNA/Acr fragments were cloned into pETDuet-1, pACYCDuet-1 and pRSFDuet-1,

respectively. They were expressed and purified similarly as the Csy complex.

Crystallization, data collection and structure determination

The AcrIF14 protein was concentrated to 12 mg/ml in 10 mM Tris–HCl pH 8.0, 200 mM NaCl and 5 mM DTT. Crystals were grown using the sitting-drop vapor diffusion method. Crystals of AcrIF14 were grown at 18°C by mixing an equal volume of the protein (12 mg/ml) with reservoir solution containing 0.1 M HEPES sodium pH 7.5, 20% (w/v) PEG 4000 and 10% (v/v) 2-Propanol. The crystals grew to full size in about three days. The crystals were cryoprotected in the reservoir solution containing 18% glycerol before its transferring to liquid nitrogen. Se-Met-labeled protein was crystallized in the same buffer. After crystal diffraction tests at home and beamlines BL17U1 and BL19U1 of the Shanghai Synchrotron Radiation Facility (SSRF), the crystal of the Se-Met-labeled protein suitable for structure determination was finally obtained.

All the data were collected at SSRF beamlines BL17U1 (24) and BL19U1 (25), integrated and scaled using the HKL2000 package (26). The initial model was solved by Autosol in PHENIX (27) and refined manually using COOT (28). The structure was further refined with PHENIX (27) using non-crystallographic symmetry and stereochemistry information as restraints. The final structure was obtained through several rounds of refinement. Data collection and structure refinement statistics are summarized in Supplementary Table S1. All of the structural illustrations were generated using the software PyMOL.

Double-stranded DNA preparation

For the *in vitro* cleavage assay and EMSA, single-stranded DNA were all purchased from Sangon, Shanghai. Single-stranded DNAs with 5′-FAM were hybridized with their complementary unlabeled single-stranded DNA with a molar ratio of 1:1.5 to obtain double-stranded DNA, and were abbreviated to $dsDNA_{SP}$ (specific) and $dsDNA_{NS}$ (non-specific). Unlabeled $dsDNA_{NS}$ was generated through the same method except that both strands were unlabeled.

Target DNA sequence (54 bp)
GGAAGCCATCCAGGTAGACGCGGACATCAA GCCCGCCGTGAAGGTGCAGCTGCT

Non-Target DNA sequence (54 bp)
AGCAGCTGCACCTTCACGGCGGGCTTGATG TCCGCGTCTACCTGGATGGCTTCC

Non-specific DNA sequence (54 bp)
GAGCGACTACGACATGAGCGCGCAGCTAAG ACCGCCCGTAGATGCGTCGAGCGT

Cryo-electron microscopy

4 μl aliquots of the Csy–AcrIF14 or Csy–AcrIF14–$dsDNA_{SP}$ complex at a concentration of ∼3 mg/ml were applied to discharged 300-mesh Quantifoil R1.2/1.3 grids (Quantifoil, Micro Tools GmbH, Germany). Grids were blotted for 3.5 s and plunged into liquid ethane using an FEI Mark IV Vitrobot operated at 4°C and 100% humidity. Micrographs were collected using a Titan Krios microscope equipped with a Gatan BioQuantum K3 Summit direct electron detector operated at 300 kV. Images were recorded with SerialEM automation software at a nominal magnification of 81 000× using super-resolution mode. The pixel size was 1.1 Å/pixel and the defocus range were set from –1.3 μm to –2.3 μm. The total dose rate on the detector was about 50 e/Å^2 with a total exposure time of 3 s. Each micrograph stack contains 32 frames.

For the Csy–AcrIF14 dataset, totally 4536 micrographs were corrected for sub-region motion correction and dose weighting using UCSF MotionCor2 (29). Gctf was used to determine the contrast transfer function (CTF) parameter and produce the CTF power spectrum (30). The 4374 CTF-corrected cryo-EM images were manually selection. 1 123 658 particles were auto-picked on micrographs with dose-weighting using RELION 3.0 (31). Two rounds of 2D classification requesting 50 classes resulted in 561 829 particles. The first round of 3D classification was done with $K = 6$ classes and regularization parameter $T = 10$, which resulted in 187 263 good particles, and the second round of 3D classification which contained 126 583 particles at the physical pixel size. 126 583 good particles were subjected to further 3D auto-refinement with C1 symmetry. The refinement resulted in an overall structure at a resolution of 3.75 Å. To further improve the resolution, we performed CTF refinement, which yielded a map at 3.43 Å resolution.

For the Csy–AcrIF14–$dsDNA_{SP}$ dataset, a total number of 5176 movie stacks were acquired. Motion correction, electron-dose weighting and 2-fold binning were done by MotionCor2. The motion-corrected images were processed similarly with the Csy–AcrIF14 dataset. A total of 1.33 million particles were auto-picked using RELION 3.0 and 594,044 particles were selected after two rounds of 2D classification. Two round of 3D classification were resulted in 386 359 good particles with $K = 5$ classes and regularization parameter $T = 10$. Finally 127 754 particles were refined and subjected to 3D classification without alignment with $K = 3$ and $T = 20$. The good classes were two rounds of CTF parameter refinement,and postprocessed separately to give final maps at 3.11 Å resolution for model building.

Model building and refinement

Atomic model of the Csy complex was obtained from the structure of the Csy complex (PDB: 6B45) and the subunits were individually fitted into the maps as a rigid-body in UCSF Chimera (32). The crystal structure of AcrIF14 was used as its model and fitted into the map and manually adjusted in COOT (28). The overall model was subjected to global refinement and minimization in real_space_refinement using PHENIX (27).

In vitro DNA cleavage assay

Non-target DNA strand with 5′-FAM fluorescein labeled was used in the *in vitro* dsDNA cleavage assay. Reactions were performed in a 20 μl system. AcrIF14 or its mutants were first incubated with Csy at 37°C in reaction buffer (20 mM HEPES pH 7.5, 100 mM KCl, 5% glycerol, 1 mM TCEP) for 30 min, and then $dsDNA_{SP}$ was added and incubated for another 30 min. And then Cas2/3 was added to a final concentration of 0.4 μM, along with which 5 mM

$MgCl_2$, 75 μM $NiSO_4$, 5 mM $CaCl_2$ and 1 mM ATP were added into the buffer. The reaction was further incubated for 15 min and quenched with the mixture of 5% SDS and 0.25 mM EDTA. In the reactions, 1 μM Csy complex, 0.4 μM Cas2/3, 0.05 μM $dsDNA_{SP}$, and varied concentrations of AcrIF14 were added. For comparing the activity between AcrIF14 and its mutants Y89A/E91A, R84A, F104A/Y105A, the AcrIF14 concentrations were set as 1, 1.5 and 2 μM. The products were separated by electrophoresis over 14% polyacrylamide gels containing 7 M urea and visualized by fluorescence imaging.

Electrophoretic mobility shift assay

Target DNA strand with 5′-FAM fluorescein labeled was used in the EMSA experiments. Reactions were performed in a 20 μl system containing 0.25 μM dsDNA, varied concentrations of Csy, Csy-Acr complexes, AcrIF14 or their mutants. All binding reactions were conducted in the buffer containing 20 mM HEPES pH 7.5, 150 mM NaCl and 5% glycerol. For the assays using Csy and Acr separately, 4 μM Csy complex was first incubated with AcrIF14 or its mutants in a concentration gradient (4/8/16/32 μM) at 37°C for 30 min in the reaction buffer mentioned above, and then 0.25 μM $dsDNA_{SP}$ or $dsDNA_{NS}$ was added and incubated for another 30 min. For the assays using the Csy-Acr complexes, the Csy/Csy–AcrIF14/Csy–AcrIF9 or their mutant complexes in a concentration gradient (0.25, 0.5, 1, 2, 4 and 8 μM) were incubated with 0.25 μM $dsDNA_{SP}$ or $dsDNA_{NS}$ at 37°C for 30 min. In competition EMSA experiments, the Csy complex or Csy–AcrIF14 (4 μM), were first incubated with 0.25 μM $dsDNA_{SP}$ at 37°C for 30 min. Then the competitive DNA ($dsDNA_{NS}$ or $ssDNA_{NS}$ with no FAM labeled) was added at increasing concentrations with the following molar ratios (1:1, 1:2, 1:4, 1:8, 1:16, 1:32) and incubated at 37°C for another 30 min. Products of the reaction were separated using 5% native polyacrylamide gels and visualized by fluorescence imaging.

Ni-pull-down assay

His-tagged Csy complex and wild-type or mutant AcrIF14 proteins were purified according to the procedure described above. 8 μM His-tagged Csy complex was first incubated with Ni-NTA resin (GenScript) in 20 μl buffer containing 20 mM HEPES pH 7.5, 150 mM NaCl and 5% glycerol at 18°C for 10 min, and then 40 μM AcrIF14 or its mutants were added in the system and incubated at 37°C for 30 min. The resins were washed three times with buffer containing 50 mM Tris, pH 8.0, 300 mM NaCl and 50 mM imidazole. The resins were then analyzed through 8–16% SDS–PAGE with Coomassie blue staining (CBS).

Gel filtration assay

The AcrIF14 protein and the gel filtration standard (BIO-RAD, Cat. #151-1901) were applied to a size-exclusion chromatography column (Superdex-75 increase 10/300 GL, GE Healthcare) equilibrated with a buffer containing 10 mM Tris–HCl pH 8.0, 200 mM NaCl and 5 mM DTT. The assays were performed with a flow rate of 0.5 ml/min and an injection volume of 1 ml for each run.

RESULTS

The crystal structure of AcrIF14

Consistent with previous results (16), AcrIF14 displays strong inhibition towards the CRISPR–Cas system in the *in vitro* cleavage assay (Figure 1A). In order to determine the mechanism underlying the immune suppression by AcrIF14, we first solved the crystal structure of AcrIF14 at 1.96 Å using single-wavelength anomalous dispersion (SAD) phasing (Supplementary Table S1 and Figure 1B and C). There is one AcrIF14 molecule in the asymmetric unit. Gel filtration chromatography also indicated that it exists as a monomer (Supplementary Figue S1A). AcrIF14 displays a two-domain structure, with an N-terminal four-helical-bundle spanning the residues from 1 to 77 (NTD), and a C-terminal mixed α/β lobe (CTD). Although Dali search (33) returned entries with structural similarities to parts of $AcrIF14^{NTD}$ (Supplementary Figue S1B), no structures with exactly the same four-helical-bundle fold as $AcrIF14^{NTD}$ have been found, suggesting that $AcrIF14^{NTD}$ represents a novel fold. The $AcrIF14^{CTD}$ consists of a three-stranded anti-parallel β sheet and a helix (α5) at the C-terminus. Dali search with the CTD showed that it is structurally most similar to part of a type II pantothenate kinase from *Staphylococcus aureus* (PDB code: 4M7X, Supplementary Figue S1C and D). However, the similar region in the type II pantothenate kinase has not been reported to be employed to engage with other proteins. Gel filtration assay showed that NTD and CTD do not co-elute with each other (Supplementary Figue S1E), suggesting a weak binding. The B-factor of the linker region of AcrIF14 suggested that the flexibility of this region is weak and NTD/CTD might function as a rigid body (Supplementary Figue S1F). Taken together, AcrIF14 folds in a two-domain architecture with strong inhibition capacity toward the CRISPR–Cas system.

The cryo-EM structure of the Csy–AcrIF14 complex

In our previous study (14), we have proved that AcrIF14 interacts with the Csy complex, suggesting that it may achieve its inhibition through the interaction. To determine the interaction mode between AcrIF14 and the Csy complex, we prepared the Csy–AcrIF14 complex and determined the structure using cryo-electron microscopy (cryo-EM) at a resolution of 3.43 Å (Figures 2 and Supplementary Figure S2, and Supplementary Table S2). Overall, the Csy complex maintains its seahorse-shape, comprising a Cas6f 'head', a heterodimeric Cas8f and Cas5f 'tail', and a hexameric Cas7f 'backbone' (Figure 2A, B). Each Cas7f subunit folds like a 'right-hand' and two AcrIF14 molecules bind between the thumb and 'extended web' domains of the Cas7.4f and Cas7.6f subunits, respectively (Figure 2C). This binding mode is reminiscent of AcrIF1 and AcrIF9, which also target these two Cas7f subunits with two copies of protein (Supplementary Figue S3A) (4,5,20,21). However, the fold of AcrIF14 is markedly distinct from those of AcrIF1 and AcrIF9 (Figure 1B and Supplementary Figure S3B, C) and AcrIF14 is in a two-domain structure compared to the single-domain proteins AcrIF1 and AcrIF9. Each AcrIF14 molecule forms extensive in-

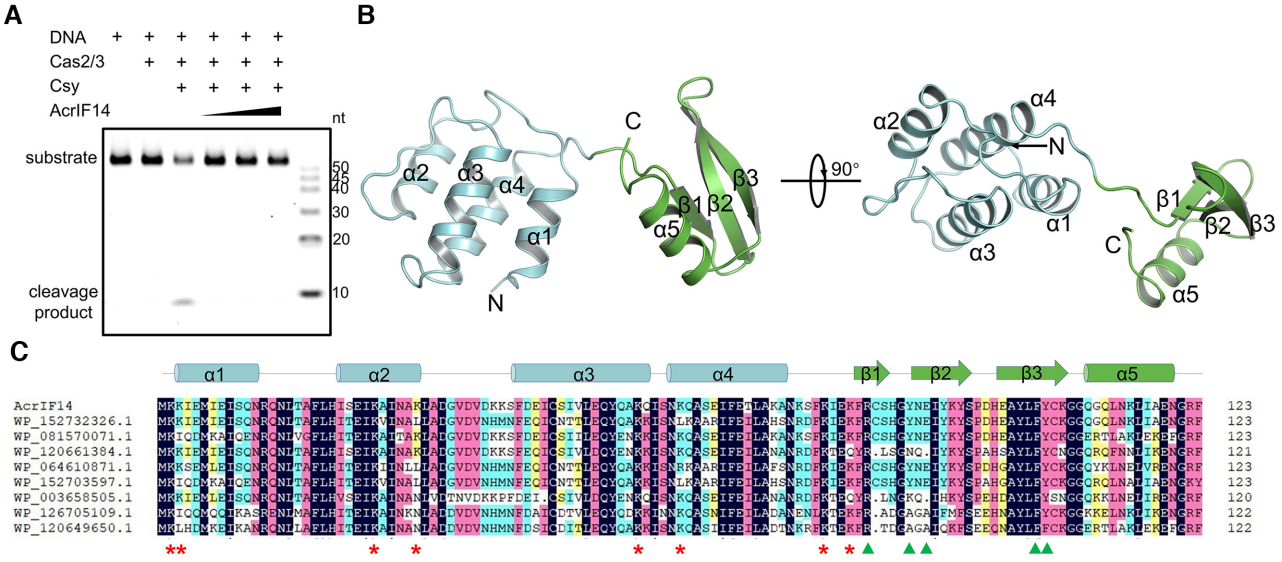

Figure 1. The crystal structure of AcrIF14. (**A**) AcrIF14 inhibits the *in vitro* DNA cleavage activity of the type I-F CRISPR system. Reactions were performed with 1 μM Csy complex, 0.4 μM Cas2/3 and 50 nM 54-bp dsDNA (5′-FAM in the non-target strand, NTS). AcrIF14 was added with concentrations of 0.5, 1 and 2 μM, respectively. The experiment was repeated three times with similar results. (**B**) The crystal structure of AcrIF14 shown in cartoon model. The NTD and CTD are shown in cyan and green, respectively. Two perpendicular views are shown with secondary structures labeled. (**C**) Sequence alignment of AcrIF14 homologs. Residues with 100% identity, over 75% identity, over 50% and over 33% identity are shaded in dark blue, pink, cyan and yellow, respectively. Secondary structural elements of AcrIF14 are shown above the sequences, colored as in Figure 1B. AcrIF14 residues highlighted in Figures 3B–D and 6A are marked with triangles and asterisks, respectively.

teractions with the thumb and 'extended web' domains of Cas7f, with a buried surface of ∼1014 Å^2. AcrIF14 interacts with the Csy complex mainly through its CTD, and its NTD is protruding out from the Csy–AcrIF14 complex (Figure 2B). The two AcrIF14 molecules are structurally similar to each other, with a root mean square deviation (RMSD) value of 0.392 Å (Supplementary Figue S3C). Moreover, they are also similar to its crystal structure, with an RMSD of 0.627 and 0.729 Å, respectively (Supplementary Figue S3D). During the preparation of this manuscript, the structure of AcrIF14 was also solved with the Csy complex by another group (34), in which the density of the AcrIF14^{NTD} in the cryoEM map was not clear enough and the NTD was not included in the final structure of AcrIF14 (PDB: 7JZZ). The structure of the CTD of AcrIF14 is largely similar between our and their study (Supplementary Figue S3D). Compared to the apo Csy complex, however, the binding of AcrIF14 induces significant conformational changes in the 'extended web' loop of the bound Cas7f subunit (Supplementary Figue S3E, F), suggesting a direct binding. Moreover, the conformation of the 'extended web' loop of Cas7.4f/7.6f in the Csy–AcrIF14 complex is also different from those in the Csy–dsDNA, Csy–AcrIF1 and Csy–AcrIF9 (Supplementary Figue S3G, H). Notably, structural comparison between the Csy–AcrIF14 and Csy–dsDNA complexes indicates that AcrIF14 competes with the complementary DNA strand to interact with the crRNA guide and the Cas7.4/7.6f subunits (Figure 2C, D), suggesting that AcrIF14 might inactivate the CRISPR–Cas system through inhibiting the hybridization of target DNA.

Detailed interactions between AcrIF14 and the Csy complex

The interaction interface between AcrIF14 and the Cas7.4/7.6f subunit can be divided into three regions, the thumb and 'extended web' domains of the Cas7f subunit, and part of the crRNA, respectively (Figure 3A). The interface of the thumb domain mainly involves polar interactions. The sidechain of R84 of AcrIF14^{CTD} forms hydrogen bonds with the carbonyl oxygen atoms of S70 and S73, and the sidechain oxygen atom of N75 of Cas7f (Figure 3B). Meanwhile, the sidechain of Y93 of AcrIF14^{CTD} is hydrogen-bonded to the sidechain of Cas7f Q77. In the interface of the 'extended web' domain, F104 and Y105 of AcrIF14 form hydrophobic interactions with the sidechains of K238, Q241 and S243 of Cas7f (Figure 3C). Apart from the interactions with the Cas7f subunit, AcrIF14 also interacts with the crRNA around the thumb domain of Cas7f. Y89 of AcrIF14.1 and AcrIF14.2 interacts with A^{16} and A^4 of the crRNA with π–π stacking, respectively (Figure 3D). Moreover, E91 of AcrIF14 also forms a potential hydrogen bond with the base of the adenine nucleotide that Y89 binds. Consistent with these structural observations, the mutations R84A, Y89A/E91A and F104A/Y105A of AcrIF14 all markedly decreased the binding between AcrIF14 and the Csy complex in the pull-down assay (Figure 3E). Furthermore, these mutations also markedly impaired the inhibition capacity of AcrIF14 (Figure 3F), suggesting the direct link between the binding affinity for the Csy complex and the inhibitory effect of AcrIF14. Taken together, AcrIF14 interacts with both the Cas7 subunit and the crRNA guide, which is important for the inhibitory capacity of AcrIF14.

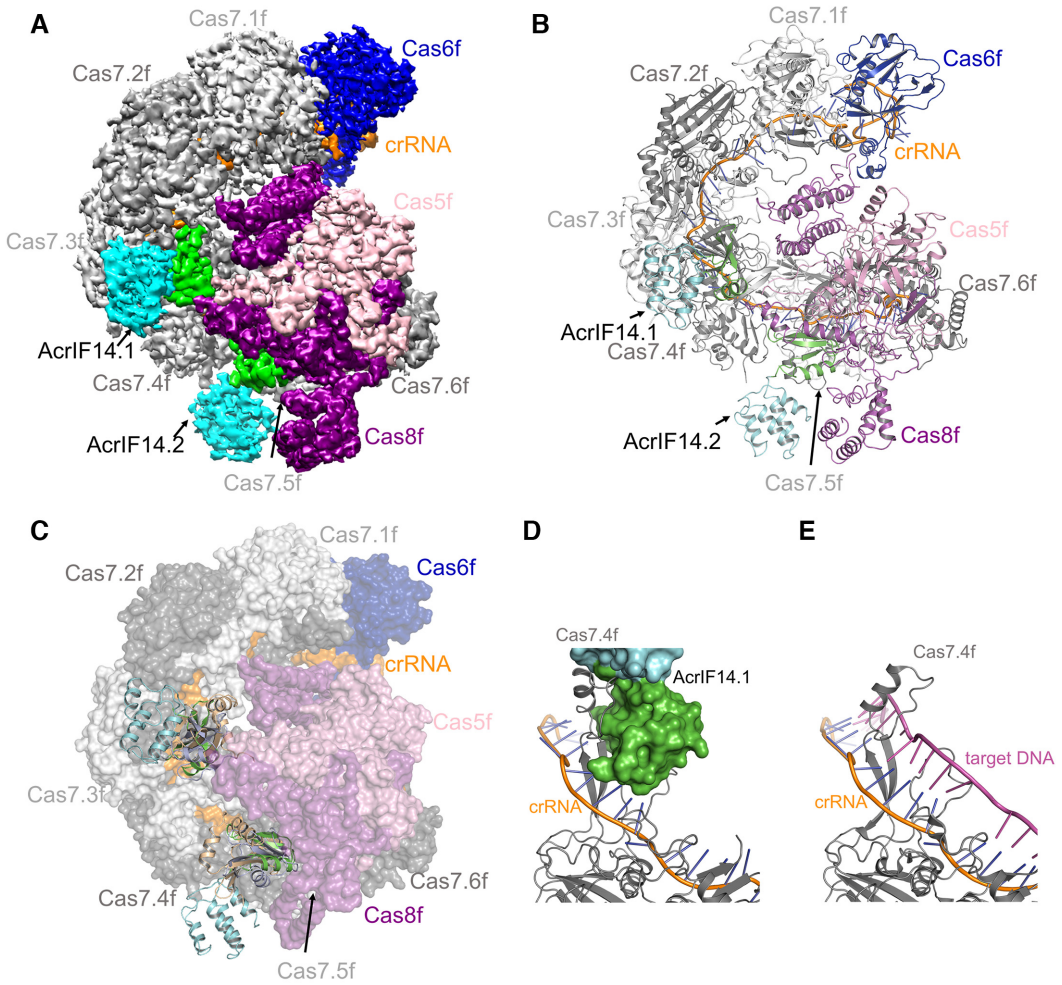

Figure 2. The cryo-EM structure of the Csy–AcrIF14 complex. (**A**) Cryo-EM map of Csy–AcrIF14 with each subunit colored respectively. Two copies of AcrIF14 are colored in cyan and green, for its NTD and CTD, respectively, as in Figure 1B. (**B**) The structure of Csy–AcrIF14 in cartoon representation with each subunit colored as in (A). (**C**) Structural superimposition among the Csy-AcrIF1/9/14 structures. Only the Csy within the Csy–AcrIF14 complex is shown in surface model and colored as in (B). AcrIF1 and AcrIF9 are shown in cartoon model and colored wheat and light blue, respectively. AcrIF14 is shown and colored as in Figure 1B. (**D**) The interactions between AcrIF14.1 and the Csy complex. AcrIF14.1 is colored as in Figure 1B and shown in surface model. (**E**) The interactions between target DNA and the Csy complex in the Csy-dsDNA structure (PDB code: 6NE0).

AcrIF14 induces strong non-specific DNA binding activity in the Csy complex

While the positioning of AcrIF1 and AcrIF9 are similar on the Csy complex and both sterically block hybridization of the target DNA to the crRNA-guide, AcrIF9 was found to exhibit another layer of inhibition through promoting the loading of non-sequence-specific dsDNA to the Csy–AcrIF9 complex (21,23). Therefore, we wondered which inhibition mechanism will be adopted by AcrIF14 or whether it will take a mechanism distinct from both of them. To test this, we performed an electrophoretic mobility shift assay (EMSA) to determine whether AcrIF14 is able to inhibit crRNA-guided interactions with target DNA. No inhibition of target dsDNA binding to the Csy complex by AcrIF14 was observed under our experimental conditions, however, a clear band with increased size appeared at a stoichiometric ratio of AcrIF14 to the Csy complex as low as 1: 1 (Figure 4A). This is reminiscent of AcrIF9, although the structures of the two proteins are highly distinct from each other (Figures 1B and S3C). To further investigate this feature of AcrIF14, we co-expressed Csy and AcrIF14, and purified them as a complex (Supplementary Figue S4). Titration experiments with both the apo Csy and Csy–AcrIF14 complex indicated that Csy–AcrIF14 binds target dsDNA (short for $dsDNA_{SP}$ hereafter) with a comparable affinity as the apo Csy (Figure 4B). We also performed an EMSA experiment using a non-specific dsDNA ($dsDNA_{NS}$) which harbors the same length and base composition as $dsDNA_{SP}$, but disordered sequence and no PAM at the corresponding site (21,23). While the apo Csy displays no $dsDNA_{NS}$ binding even at a 16-fold concentration of DNA, the Csy–AcrIF14 complex could form a ternary complex with $dsDNA_{NS}$ with as low as 2-fold concentration (Figure 4C). Notably, AcrIF14 itself displays no binding to either dsDNA molecule among the same range of concentrations (Supplementary Figue S5). Furthermore,

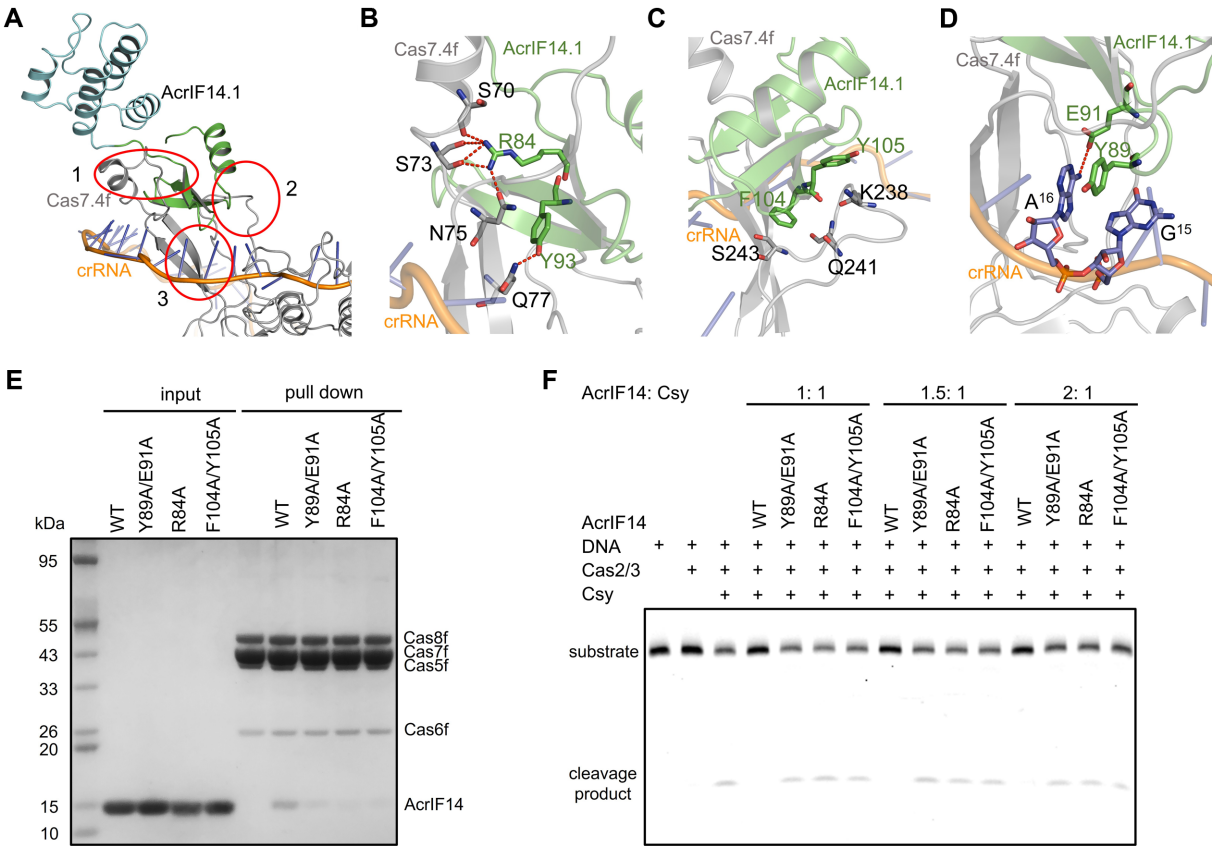

Figure 3. Detailed interactions between AcrIF14 and the Csy complex. (**A**) Overview of the binding between AcrIF14.1 and the Csy complex. The three interfaces are marked in circles. (**B–D**) Close-up views of the interfaces marked in circles in (A), with B, C, and D representing interface 1, 2 and 3, respectively. Interacting residues are shown in sticks, and polar interactions are shown as red dashed lines. (**E**) Ni-pull-down assay of the AcrIF14 mutants to disrupt the binding with the Csy complex. 8 μM His-tagged Csy complex was incubated with 40 μM AcrIF14 or its mutants, analyzed through SDS-PAGE stained with CBS. The experiment was repeated three times with similar results. (**F**) The interaction mutations of AcrIF14 decreased its inhibition capacity in the *in vitro* DNA cleavage activity. Reactions were performed with 1 μM Csy complex, 0.05 μM 54-bp dsDNA (5′-FAM in the NTS) and 0.4 μM Cas2/3. AcrIF14 or its mutants were added with concentrations of 1, 1.5 and 2 μM, respectively, when needed. The experiment was repeated three times with similar results.

we performed competition EMSA experiments to investigate whether the binding sites of $dsDNA_{SP}$ overlap with those of $dsDNA_{NS}$ on the Csy–AcrIF14 complex. FAM-labeled dsDNA was premixed with Csy or Csy–AcrIF14 respectively, and then unlabeled dsDNA was added in increasing concentrations. While no decrease in binding to $dsDNA_{SP}$ was observed for the apo Csy complex, increased levels of free $dsDNA_{SP}$ was observed with increasing concentrations of $dsDNA_{NS}$ in the reactions of Csy–AcrIF14 complex (Figure 4D). Similar results were obtained for Csy–AcrIF14 in the competition experiment with reverse incubation order (Figure 4E). This suggests that $dsDNA_{SP}$ and $dsDNA_{NS}$ compete for the same site on the Csy–AcrIF14 complex for binding. Notably, mutations of the Csy-interacting residues of AcrIF14 also impaired or abolished the induction of the Csy–AcrIF14–dsDNA ternary complex (Figure 4F), indicating that the formation of the ternary complex depends on the interactions between the Csy complex and AcrIF14. Taken together, AcrIF14 promotes non-specific DNA binding activity in the Csy complex, which is dependent on the formation of the Csy–AcrIF14 complex.

The cryo-EM structure of the Csy–AcrIF14–$dsDNA_{SP}$ complex

To determine how the Csy–AcrIF14 complex recruits $dsDNA_{SP}$, we purified the Csy–AcrIF14–$dsDNA_{SP}$ complex through incubating the Csy–AcrIF14 complex with $dsDNA_{SP}$ and solved its structure at a resolution of 3.11 Å (Figure 5A and Supplementary Figure S6, and Supplementary Table S2). While the density of the backbone and the tail region of the Csy complex is well-defined and could be accurately modeled, no density is observed for the Cas6f subunit or the crRNA 3′ stem loop at the head region, possibly due to its flexibility, similar to what was reported previously (5,6). For the $dsDNA_{SP}$, interestingly, density is only visible to build a 13-bp dsDNA at the PAM-proximal region, including the PAM (G-C/G-C) sequence (Figure 5B). Different from the large conformational change between the structures of Csy and Csy–dsDNA (7), the structure of the Csy–AcrIF14–$dsDNA_{SP}$ complex does not show overall conformational change compared to that of Csy–AcrIF14, with an RMSD of 1.428 Å. The binding mode of the part of $dsDNA_{SP}$ in the Csy–AcrIF14 complex is similar to what was reported for the Csy–dsDNA structure (5,7),

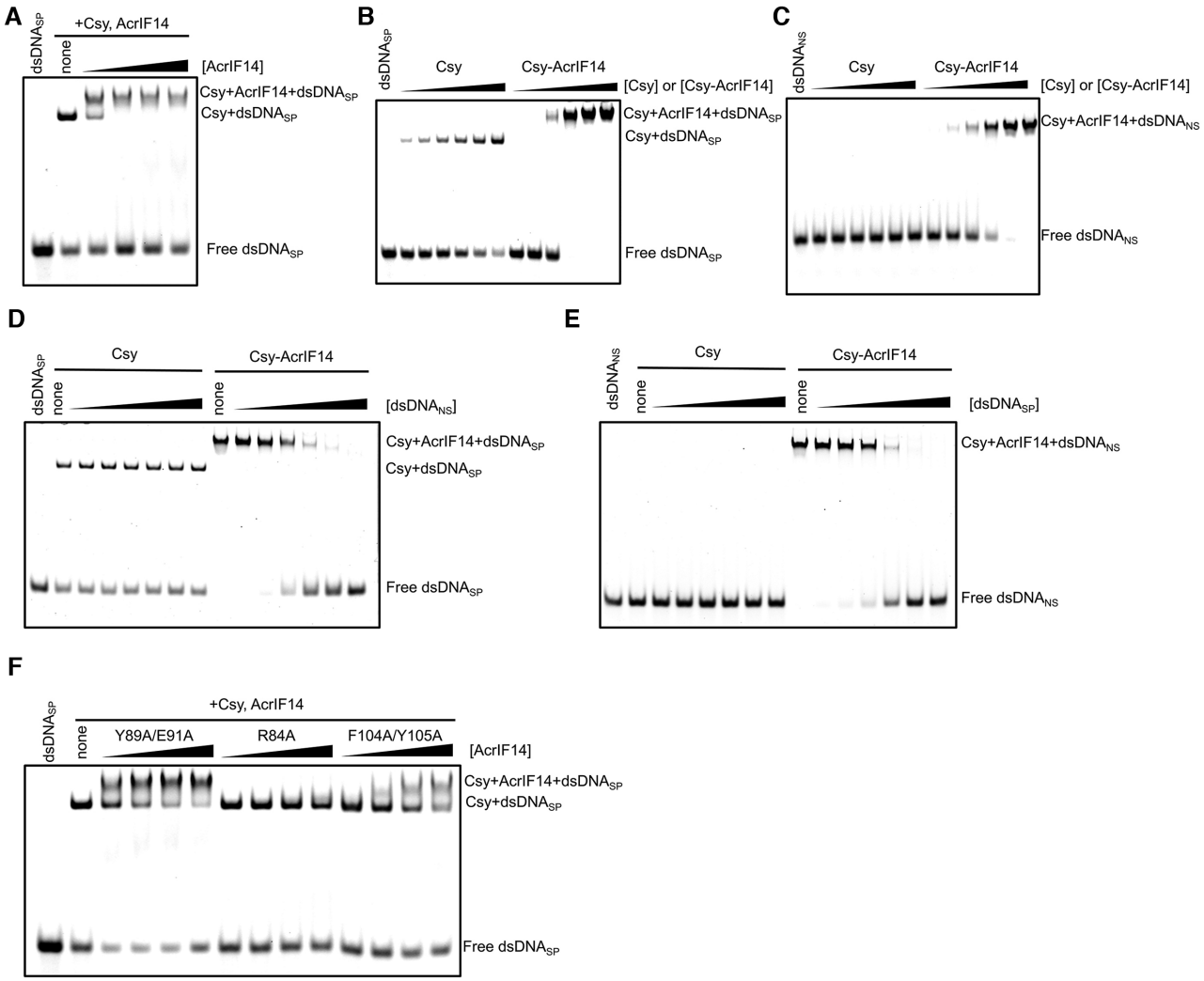

Figure 4. AcrIF14 induces strong non-specific DNA binding activity in the Csy complex. (**A**) EMSA used to test the effects of AcrIF14 on the binding between Csy and $dsDNA_{SP}$. Reactions were performed with 4 μM Csy complex, 0.25 μM 54-bp dsDNA (5′ -FAM in the target DNA strand, TS), and AcrIF14 concentrations of 4, 8, 16 and 32 μM following the order indicated by the black triangle. (**B**, **C**) EMSA used to test the $dsDNA_{SP}$/$dsDNA_{NS}$ binding of the Csy and Csy–AcrIF14 complex. Increasing concentrations of Csy or Csy–AcrIF14 complex (0.25/0.5/1/2/4/8 μM) were added to 0.25 μM 54-bp $dsDNA_{SP}$ (5′-FAM in the TS) or $dsDNA_{NS}$ (5′-FAM in the non-specific DNA strand). (D, E) Competition EMSA to test the binding sites of $dsDNA_{SP}$ and $dsDNA_{NS}$. (**D**) 4 μM Csy or Csy–AcrIF14 complex was incubated with 0.25 μM 54-bp $dsDNA_{SP}$ (5′ -FAM in the TS), then increasing concentrations of unlabeled $dsDNA_{NS}$ (0.25/0.5/1/2 /4/8 μM) were added. (**E**) The procedure was the same as (D), except that $dsDNA_{NS}$ was 5′-FAM labeled and incubated first, and unlabeled $dsDNA_{SP}$ was added. (**F**) The interaction mutants of AcrIF14 disrupt its ability to induce non-sequence-specific DNA binding. Reactions were performed in the same system as (A), except that AcrIF14 mutants but not WT AcrIF14 were added. All the above experiments were repeated three times with similar results.

except that the density of the A^1 in the target strand is not clear enough to confirm its base-pairing with U^1 of the cr-RNA (Figure 5B). The $dsDNA_{SP}$ duplex is separated at the A^1(TS)–T^1(NTS) position, but no density is observed for the following nucleotides. In the Csy–AcrIF14–$dsDNA_{SP}$ structure, consistent with previous studies (5,7), K247 and N250 of the Cas8f subunit are involved in $dsDNA_{SP}$ binding (Figure 5B). In our previous study, we also confirmed that the K247E and N250D mutations of the Cas8f subunit both abolished the $dsDNA_{SP}$ binding of the Csy complex (14). To investigate the roles of these two residues in dsDNA binding by the Csy–AcrIF14 complex, we purified Csy–AcrIF14 complexes in which the Csy complex included either the Cas8f K247E or the Cas8f N250D mutation. These two Csy–AcrIF14 mutants both showed almost no binding towards either $dsDNA_{SP}$ or $dsDNA_{NS}$ (see Figures 4B, C and 5C), suggesting the essential role of the PAM recognition loop (the K wedge) in the non-specific DNA binding induced by AcrIF14. This is also consistent with the notion that the binding sites are overlapping for $dsDNA_{SP}$ and $dsDNA_{NS}$ in the Csy–AcrIF14 complex. During the process of target dsDNA binding by the Csy complex, PAM recognition is followed by the unwinding of the dsDNA, known as R-loop formation, which allows hybridization of the target DNA strand with the crRNA spacer (35). In a previous study, an R-loop binding channel (RBC) comprising positively charged residues of Cas8f and Cas5f was identified in the Csy complex, and proposed to make sequence-

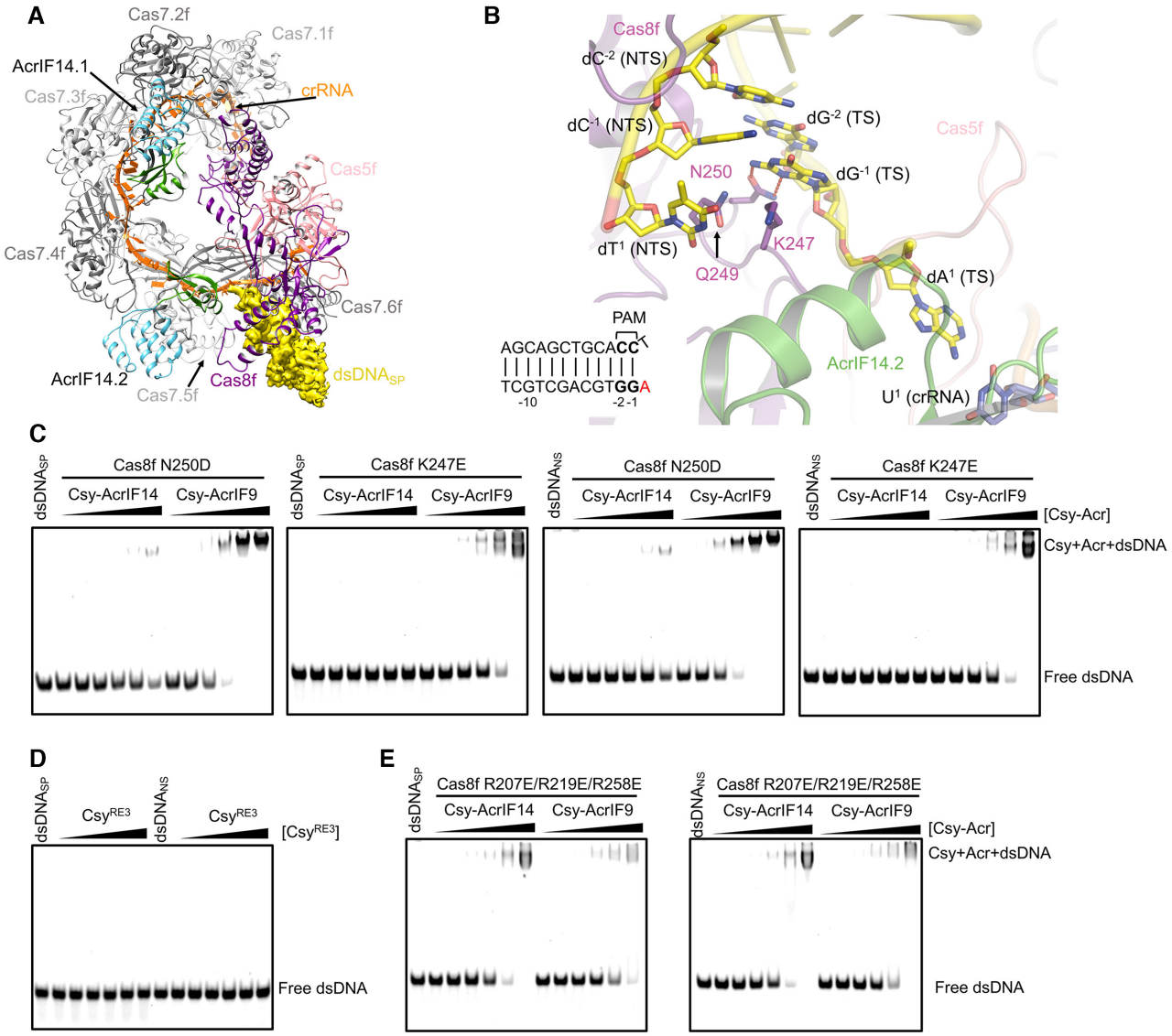

Figure 5. The PAM recognition loop and RBC of Cas8f are involved in non-specific DNA binding. (**A**) Model of the Csy–AcrIF14–dsDNA$_{SP}$ complex. Csy–AcrIF14 is shown in cartoon representation and the density of the dsDNA$_{SP}$ is shown. (**B**) Close-up view of the binding site of dsDNA$_{SP}$ within the Csy–AcrIF14–dsDNA$_{SP}$ complex. Hydrogen bonds are shown as red dashed lines. A schematic drawing of the partial dsDNA with visible density is shown in the left bottom. (**C**) EMSA used to test the effects of N250D and K247E mutations of the Cas8f subunit on the non-specific DNA binding activity induced by AcrIF14 or AcrIF9. Reactions were performed in the same system as Figure 4B, C. (**D**, **E**) EMSA used to test the effects of R207E/R219E/R258E mutations of the Csy complex in the non-specific DNA binding activity induced by AcrIF14 or AcrIF9. Reactions were performed in the same system as Figure 4B, C. The experiments in C–E were repeated three times with similar results.

independent interactions with the R-loop (7). Since the positively charged residues of RBC within the central domain of Cas8f are near to the bound dsDNA$_{SP}$ (Supplementary Figue S7), we hypothesized that these residues might also be involved in non-specific DNA binding. To test this, we purified a Csy–AcrIF14 complex, in which the Csy complex bears R207E/R219E/R258E mutations in its Cas8f subunit (short for Csy^{RE3} hereafter). The Csy^{RE3} complex itself displayed no binding to either dsDNA$_{SP}$ or dsDNA$_{NS}$ under the Csy concentrations used in this study (Figure 5D). Notably, the Csy^{RE3}–AcrIF14 complex also displayed markedly reduced binding to both dsDNA$_{SP}$ and dsDNA$_{NS}$ (Figure 5E). Therefore, both the PAM recognition loop and the RBC of the Cas8f subunit mediate the non-specific DNA binding induced by AcrIF14.

A positively charged surface of AcrIF14^{NTD} is involved in non-specific DNA binding and related to the inhibitory capacity of AcrIF14

Since the Csy complex itself does not bind dsDNA$_{NS}$ (Figure 4C) and the binding features of dsDNA$_{SP}$ are also different between the apo Csy and Csy–AcrIF14 complex (Figure 4D), the PAM recognition loop and the RBC of the Cas8f subunit identified above should not be sufficient for this non-specific DNA binding. Therefore, we moved on to

investigate which part of AcrIF14 is involved in this binding. Since AcrIF14^{CTD} is mainly involved in interactions with the Csy complex, we proposed that AcrIF14^{NTD} might be responsible for non-sequence-specific DNA binding. An investigation of the crystal structure of AcrIF14 identified a surface of the NTD with several large positively charged patches, while the other surface of the NTD mainly comprises of hydrophobic and negatively charged residues (Figure 6A). Based on the structure of AcrIF14, we performed a structure-guided mutagenesis of the patches with positive charge within the NTD of AcrIF14 (Figures 1C and 6A) by mutating lysine residues to glutamates. EMSA experiments with both dsDNA$_{SP}$ and dsDNA$_{NS}$ were performed to determine whether any mutations will impair the ability of AcrIF14 to induce the formation of Csy–AcrIF14–dsDNA ternary complex. In reactions with both dsDNA$_{SP}$ and dsDNA$_{NS}$, all the above mutations markedly decreased the formation of the ternary complex (Figure 6B). These mutations also turned AcrIF14 into an Acr with majorly the 'competing' function to sterically block target DNA binding (Figure 6B). Consistently, EMSA experiments with the Csy–AcrIF14 complexes in which AcrIF14 contains these mutations also showed markedly reduced or no binding to dsDNA$_{SP/NS}$ (Supplementary Figue S8). Notably, none of these mutants impaired the interactions with the Csy complex (Supplementary Figue S9). Then we moved on to determine whether these AcrIF14 mutants will display weaker inhibition in the *in vitro* cleavage assays. Here, besides conventional *in vitro* cleavage assay (Figure 6C, D), we also tested another reaction system by including an excess of non-specific DNA into the reaction which might increase the importance of these AcrIF14 residues for function (Figure 6E, F). The results showed that all the mutants displayed decreased inhibitory activity in both cleavage experiments, compared to WT AcrIF14 (Figure 6C–F and Supplementary Figure S10). Together, AcrIF14 induces non-specific DNA binding through the electropositive patches in its NTD, which is essential for the inhibitory capacity of AcrIF14.

AcrIF14 and AcrIF9 do not induce non-specific DNA binding by the same mechanism

Since AcrIF14 and AcrIF9 engage the same subunits of the Csy complex and both induce non-specific DNA binding to the Csy complex, we then compared the activities of the two Acr proteins in multiple aspects to determine whether they adopt the same mechanism. It was reported that multiple Csy–AcrIF9 complexes bind to non-specific DNA based on the supershift band of the Csy–AcrIF9–dsDNA (23). Comparison between the EMSA results of Csy–AcrIF14 and Csy–AcrIF9 showed that the Csy–Acr–dsDNA$_{SP}$/dsDNA$_{NS}$ complexes display similar mobilities for the two Acrs, suggesting that there might also be multiple Csy–AcrIF14 complexes on the dsDNA (Supplementary Figue S11). For specific ssDNA, however, while the DNA bound by the Csy–AcrIF9 and the apo Csy migrated at a similar position (23), the DNA bound by the Csy–AcrIF14 displayed a slower mobility and was smeared at a stoichiometric ratio of Csy–AcrIF14 to DNA of 8: 1 (Figure 7A). The difference between the mobilities of the ssDNA bound by Csy–AcrIF14 and Csy–AcrIF9 is more prominent when ssDNA$_{NS}$ was used (Figure 7A). Competition EMSA experiments with ssDNA showed that ssDNA$_{NS}$ does not compete ssDNA$_{SP}$ off from the Csy–AcrIF9 complex among the incubation ratios (Figure 7B), consistent with a previous study (23). For Csy–AcrIF14, at least three bands corresponding to Csy–AcrIF14–ssDNA$_{SP}$ complexes were observed, in which the lowest band at a position slightly higher than Csy–ssDNA$_{SP}$ appeared and its intensity increased with the increasing concentrations of ssDNA$_{NS}$ (Figure 7C). In addition, a small quantity of ssDNA$_{SP}$ started to be competed off by ssDNA$_{NS}$ when the ratio of ssDNA$_{NS}$/ssDNA$_{SP}$ was 32:1. These results suggested that Csy–AcrIF14 and Csy–AcrIF9 interact with ssDNA differently. To further investigate the DNA binding mechanism of Csy–AcrIF14, we also performed the competition experiment in reverse, which showed that ssDNA$_{NS}$ is competed off with the addition of ssDNA$_{SP}$ (Figure 7D). Taken together, the above results indicated that while Csy–AcrIF14 may exhibit distinct affinities to ssDNA$_{SP}$ during the formation of different types of Csy–AcrIF14–ssDNA$_{SP}$ complexes and the stability of the different Csy–AcrIF14-ssDNA$_{SP}$ complexes vary (Figure 7C, D), Csy–AcrIF14 exhibits a higher affinity for ssDNA$_{SP}$ than ssDNA$_{NS}$.

Next, we tested the effect of the RBC mutations on the dsDNA binding activity of Csy-AcrIF9 also using the Csy^{RE3} mutant. Titration experiments showed that the Csy^{RE3}–AcrIF9 also displayed reduced binding to both dsDNA$_{SP}$ and dsDNA$_{NS}$ compared to Csy-AcrIF9 (see Figure 5E), suggesting that this region of the Csy complex also participates in the non-specific DNA binding of the Csy-AcrIF9 complex. Consistently, in a very recent study, another Csy mutant Csy$^{Cas8\text{-}RK}$ bearing R207A/K216A/R224A mutations of the Cas8f subunit also showed reduced binding to dsDNA$_{SP}$ and dsDNA$_{NS}$ when complexed with AcrIF9 (23). Finally, the effect of the mutations of the PAM recognition loop of the Csy complex was tested on the Csy–AcrIF9 complex. Surprisingly, for AcrIF9, the Cas8f N250D mutation did not cause markedly decreased binding of either dsDNA$_{SP}$ or dsDNA$_{NS}$, but the Cas8f K247E mutation resulted in reduced non-specific DNA binding (Figure 5C). The Csy–AcrIF9–dsDNA$_{NS}$ structure (21) also shows that the binding site of dsDNA$_{NS}$ is away from the PAM recognition loop and is also different from that of dsDNA$_{SP}$ in the Csy–AcrIF14–dsDNA$_{SP}$ complex (Supplementary Figue S12). This suggests that in AcrIF9-induced non-specific DNA binding, the PAM recognition loop might play a different role from that in AcrIF14-induced DNA binding. Taken together, AcrIF14 and AcrIF9 display distinct mechanisms in terms of ssDNA binding and the role of the PAM recognition loop of the Csy complex in Acr-induced non-specific DNA binding.

DISCUSSION

In this study, we uncovered the dual functions of AcrIF14 during the inhibition of type I-F CRISPR system. On the one hand, two AcrIF14 molecules engage the Cas7.4f and Cas7.6f subunits to inhibit target DNA binding, which was also revealed by the previous structural study of AcrIF14 (34). On the other hand, AcrIF14 also endows the Csy com-

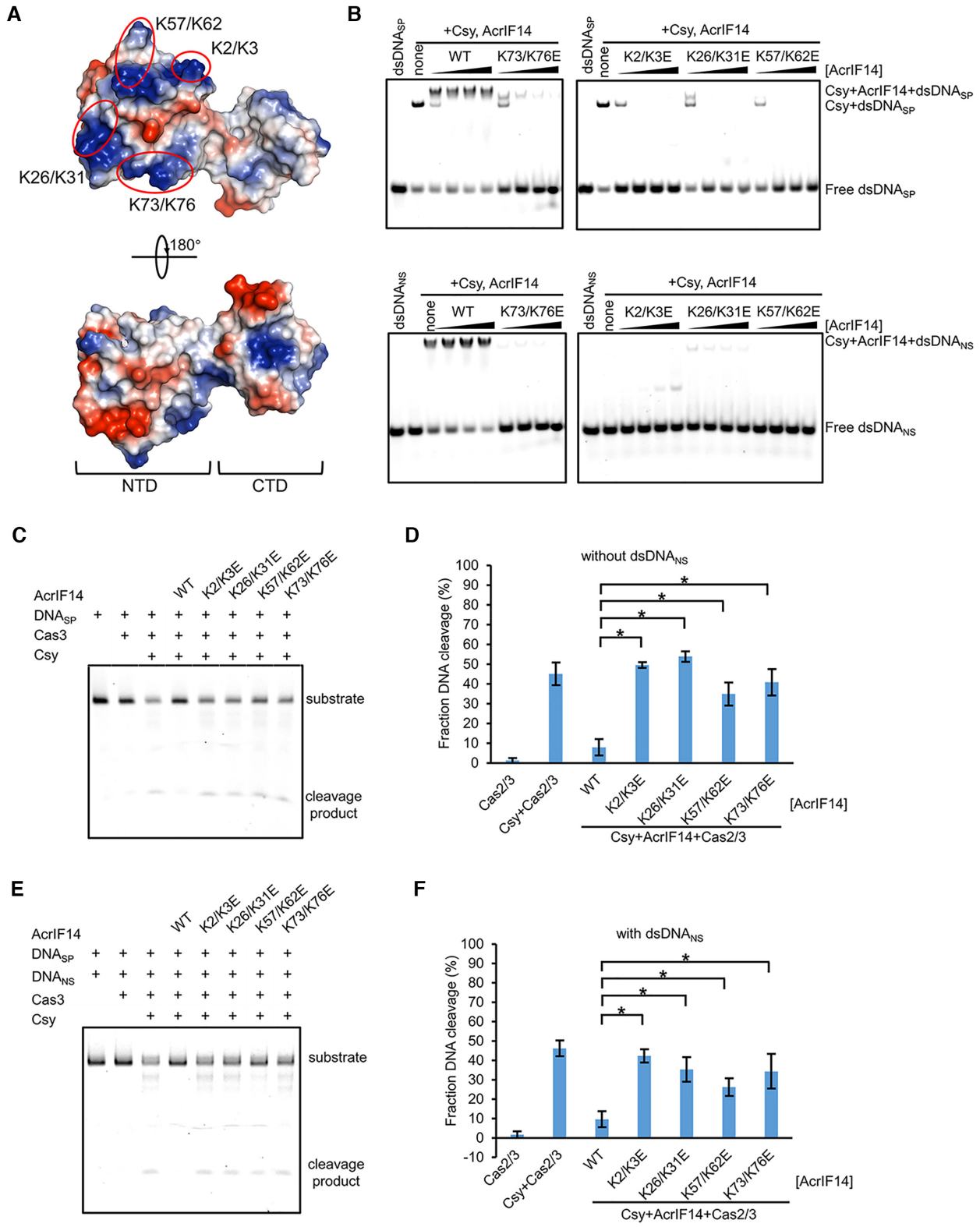

Figure 6. Non-specific DNA binding induced by AcrIF14 is related to its inhibitory capacity. (**A**) AcrIF14 is shown in electrostatic surface model. Four patches of residues with positive charges are marked with circles. (**B**) Mutations of the electropositive patches on AcrIF14^{NTD} disrupt the non-specific DNA binding activity. Reactions were performed in the same system as Figure 4A. The experiment was repeated three times with similar results. (**C**) and (**E**) Mutations of the electropositive patches on AcrIF14^{NTD} decreased its inhibition capacity in the *in vitro* DNA cleavage activity. Reactions were performed with 1 μM Csy complex, 0.05 μM 54-bp dsDNA$_{SP}$ (5′ -FAM in the NTS), 0.4 μM Cas2/3 and 1 μM AcrIF14 or its mutants (D). 1 μM 54-bp dsDNA$_{NS}$ was additionally included in the system in (E). The experiments were repeated three times with similar results and representative results are shown. (**D** and **F**) Quantitative results of the experiment in (C) and (E), respectively. Error bars represent SD; $n = 3$. Paired t test was performed (*$P < 0.05$).

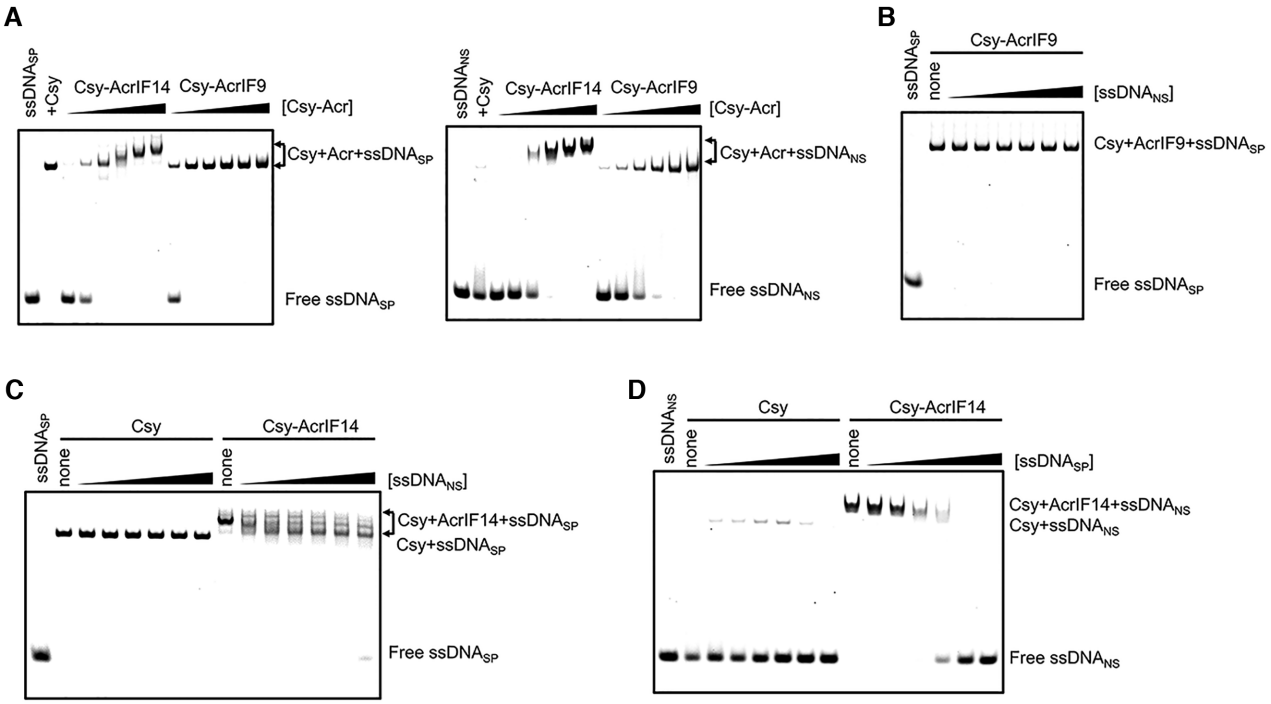

Figure 7. AcrIF14 and AcrIF9 do not induce non-specific DNA binding by the same mechanism. (**A**) EMSA used to test the ssDNA$_{SP}$/ssDNA$_{NS}$ binding to the Csy–AcrIF14 and Csy–AcrIF9 complex. Increasing concentrations of Csy–AcrIF14 or Csy–AcrIF9 complex (0.25/0.5/1/2/4/8 μM) were added to 0.25 μM ssDNA$_{SP}$ (5′-FAM in the TS) or ssDNA$_{NS}$ (5′-FAM in the non-specific DNA strand). (**B**) Competition EMSA to test the ssDNA binding of Csy–AcrIF9. Reactions were performed in the same system as Figure 4D, except that ssDNA$_{SP}$ and ssDNA$_{NS}$ but not dsDNA$_{SP}$ and dsDNA$_{NS}$ were added. (**C**, **D**) Competition EMSA to test the binding sites of ssDNA$_{SP}$ and ssDNA$_{NS}$ by Csy–AcrIF14. Reactions were performed in the same system as Figure 4D and E, except that ssDNA$_{SP}$ and ssDNA$_{NS}$ but not dsDNA$_{SP}$ and dsDNA$_{NS}$ were added. All the above experiments were repeated three times with similar results.

plex with the ability to interact with non-sequence-specific DNA molecules. Along with AcrIF9, our study suggested that Acr-induced non-specific DNA sequestration might be more prevalent in the suppression strategies of Acr than previously thought. It is very interesting that so many features of the activities of AcrIF9 and AcrIF14 are similar, despite no sequence or structural similarity. Therefore, it could be taken as a striking example of convergent evolution and may also represent 'the Achilles' heel' in the Csy complex. Interestingly, the dsDNA binding ability of a type II Acr, AcrIIA11, was dramatically improved by its interaction with Cas9 (36), suggesting that this strategy might also be utilized by Acrs of Class II CRISPR–Cas systems. Notably, the effect of inducing non-specific DNA binding by Acrs would be more prominent for inhibition in bacteria than in the *in vitro* cleavage assay, in which only target DNA is included. Supporting this, AcrIF9 mutants with reduced induction of non-specific DNA binding also showed decreased *in vivo* Acr activity (23).

During the interference step, the Csy complex first conducts target search through rapid association and dissociation with non-target dsDNA (37). Encountering with a PAM sequence provides weak, but specific interactions between the Csy complex and target DNA, which destabilizes the DNA duplex and thereby facilitate the following crRNA-guided strand invasion (37). A stable and functional Csy–dsDNA complex, which could further recruit the Cas2/3 nuclease, will be formed when the protospacer sequence is present in the target DNA and hybridization between the target DNA strand and the crRNA occurs. However, if the PAM adjacent sequence is not complementary to the crRNA, then the Cascade-PAM interaction is transient and the search continues (38). It should have been also the case when the target-DNA-binding thumb domains of Cas7.4f/7.6f of the Csy complex are engaged by Acrs such as AcrIF1/9/14. However, in this study, we showed that the Csy–AcrIF14 complex is able to bind both dsDNA$_{SP}$ and dsDNA$_{NS}$ at similar sites, suggesting that this is a non-sequence-specific binding (Figure 4B-D) and the PAM sequence is not essential for the bound dsDNA. Interestingly, we identified the essential role of the PAM recognition loop of Cas8f (K247 and N250) in AcrIF14-induced non-specific DNA binding for both dsDNA$_{SP}$ and dsDNA$_{NS}$. Moreover, we also showed that several electropositive patches in the NTD of AcrIF14 are essential for non-specific DNA binding (both dsDNA$_{SP}$ and dsDNA$_{NS}$). While the interaction details of dsDNA$_{NS}$ in the Csy–AcrIF14 complex cannot be exactly the same as that of dsDNA$_{SP}$, the interaction between Csy–AcrIF14 and dsDNA$_{NS}$ could be generally explained by the Csy–AcrIF14–dsDNA$_{SP}$ structure. Considering the structural flexibility of the AcrIF14^{NTD}, our results lead to a very interesting model: First, AcrIF14 engages the Cas7.4f and Cas7.6f subunits of the Csy complex and form a stable Csy–AcrIF14 complex through its CTD. This prevents hybridization between target DNA and the crRNA even if a target DNA sequence with PAM and

protospacer sequence is encountered. The Csy–AcrIF14 complex then searches DNA by rapid association, however, the electropositive patches on the structurally flexible NTD of AcrIF14 might facilitate DNA binding with the help of the PAM recognition loop and the RBC in the Cas8f central domain, no matter the PAM and the adjacent protospacer sequences are present or not. Interestingly, mutations of all the lysine residues on the positively charged surface of $AcrIF14^{NTD}$ each severely disrupt the induced non-specific DNA binding, suggesting that the overall charge of this surface but not specific residues, might be responsible for the DNA binding. For AcrIF9-induced non-specific DNA binding, the mechanism might be analogous in some aspects but not the same, since the Cas8f N250D and K247E mutations, which respectively almost abolished DNA binding both in Csy and Csy–AcrIF14 complex (Figure 5C), caused no decrease or weak decrease in AcrIF9-induced non-specific DNA binding, respectively. Future studies should be conducted to investigate whether other Acrs also induce non-specific DNA sequestration and their underlying mechanisms.

DATA AVAILABILITY

The accession number for the coordinate and structure factor of AcrIF14 is PDB: 7DU0. Cryo-EM reconstructions of Csy–AcrIF14 and Csy–AcrIF14–$dsDNA_{SP}$ complexes have been deposited in the Electron Microscopy Data Bank under the accession numbers EMD-31058 and EMD-31059, respectively. Coordinates for atomic models of Csy–AcrIF14 and Csy–AcrIF14–$dsDNA_{SP}$ have been deposited in the Protein Data Bank under the accession numbers 7ECV and 7ECW, respectively.

SUPPLEMENTARY DATA

Supplementary Data are available at NAR Online.

ACKNOWLEDGEMENTS

We thank the cryo-EM facilities of Southern University of Science and Technology for providing the facility support. We would like to thank the staff at beamlines BL17U1 and BL19U1 of the Shanghai Synchrotron Radiation Facility for their assistance with data collection. We would like to thank the Tsinghua University Branch of China National Center for Protein Sciences Beijing and Shilong Fan for providing facility support for X-ray diffraction of the crystal samples.

Author contributions: Y.F. designed and supervised the project. X.L., Y. Xiu, L.H., Y. Xie and L.Y. purified the proteins, performed the biochemical experiments supervised by Y.Z. and Y.F.. T.G. purified the proteins, grew and optimized the crystals and collected the diffraction data. Y.F. solved the crystal structure. L.Z. collected the cryoEM data and solved the structure with the help of W.W., supervised by M.Y. and P. W.. Y.F. analyzed the data and wrote the paper with the help of all the authors.

FUNDING

National Natural Science Foundation of China [31822012, 32000901]; National Key Research and Development Program of China [2017YFA0506500, 2019YFC1200500, 2019YFC1200502]; Beijing Nova program; Fundamental Research Funds for the Central Universities [XK1802-8]. Funding for open access charge: National Natural Science Foundation of China; National Key Research and Development Program of China.

Conflict of interest statement. None declared.

REFERENCES

1. Barrangou,R., Fremaux,C., Deveau,H., Richards,M., Boyaval,P., Moineau,S., Romero,D.A. and Horvath,P. (2007) CRISPR provides acquired resistance against viruses in prokaryotes. *Science*, **315**, 1709–1712.
2. Jore,M.M., Brouns,S.J. and van der Oost,J. (2012) RNA in defense: CRISPRs protect prokaryotes against mobile genetic elements. *Cold Spring Harb. Perspect. Biol.*, **4**, a003657.
3. Makarova,K.S., Wolf,Y.I., Iranzo,J., Shmakov,S.A., Alkhnbashi,O.S., Brouns,S.J.J., Charpentier,E., Cheng,D., Haft,D.H., Horvath,P. *et al.* (2020) Evolutionary classification of CRISPR–Cas systems: a burst of class 2 and derived variants. *Nat. Rev. Microbiol.*, **18**, 67–83.
4. Chowdhury,S., Carter,J., Rollins,M.F., Golden,S.M., Jackson,R.N., Hoffmann,C., Nosaka,L., Bondy-Denomy,J., Maxwell,K.L., Davidson,A.R. *et al.* (2017) Structure reveals mechanisms of viral suppressors that intercept a CRISPR RNA-guided surveillance complex. *Cell*, **169**, 47–57.
5. Guo,T.W., Bartesaghi,A., Yang,H., Falconieri,V., Rao,P., Merk,A., Eng,E.T., Raczkowski,A.M., Fox,T., Earl,L.A. *et al.* (2017) Cryo-EM structures reveal mechanism and inhibition of DNA targeting by a CRISPR–Cas surveillance complex. *Cell*, **171**, 414–426.
6. Peng,R., Xu,Y., Zhu,T., Li,N., Qi,J., Chai,Y., Wu,M., Zhang,X., Shi,Y., Wang,P. *et al.* (2017) Alternate binding modes of anti-CRISPR viral suppressors AcrF1/2 to Csy surveillance complex revealed by cryo-EM structures. *Cell Res.*, **27**, 853–864.
7. Rollins,M.F., Chowdhury,S., Carter,J., Golden,S.M., Miettinen,H.M., Santiago-Frangos,A., Faith,D., Lawrence,C.M., Lander,G.C. and Wiedenheft,B. (2019) Structure reveals a mechanism of CRISPR-RNA-guided nuclease recruitment and Anti-CRISPR viral mimicry. *Mol. Cell*, **74**, 132–142.
8. Hwang,S. and Maxwell,K.L. (2019) Meet the anti-CRISPRs: widespread protein inhibitors of CRISPR–Cas systems. *CRISPR J*, **2**, 23–30.
9. Davidson,A.R., Lu,W.T., Stanley,S.Y., Wang,J., Mejdani,M., Trost,C.N., Hicks,B.T., Lee,J. and Sontheimer,E.J. (2020) Anti-CRISPRs: protein inhibitors of CRISPR–Cas systems. *Annu. Rev. Biochem.*, **89**, 309–332.
10. Wiegand,T., Karambelkar,S., Bondy-Denomy,J. and Wiedenheft,B. (2020) Structures and strategies of anti-CRISPR-mediated immune suppression. *Annu. Rev. Microbiol.*, **74**, 21–37.
11. Bondy-Denomy,J., Pawluk,A., Maxwell,K.L. and Davidson,A.R. (2013) Bacteriophage genes that inactivate the CRISPR/Cas bacterial immune system. *Nature*, **493**, 429–432.
12. Dong,L.Y., Guan,X.Y., Li,N.N., Zhang,F., Zhu,Y.W., Ren,K., Yu,L., Zhou,F.X., Han,Z.F., Gao,N. *et al.* (2019) An anti-CRISPR protein disables type V Cas12a by acetylation. *Nat. Struct. Mol. Biol.*, **26**, 308–314.
13. Knott,G.J., Thornton,B.W., Lobba,M.J., Liu,J.J., Al-Shayeb,B., Watters,K.E. and Doudna,J.A. (2019) Broad-spectrum enzymatic inhibition of CRISPR–Cas12a. *Nat. Struct. Mol. Biol.*, **26**, 315–321.
14. Niu,Y., Yang,L., Gao,T., Dong,C., Zhang,B., Yin,P., Hopp,A.K., Li,D., Gan,R., Wang,H. *et al.* (2020) A Type I-F Anti-CRISPR protein inhibits the CRISPR–Cas surveillance complex by ADP-Ribosylation. *Mol. Cell*, **80**, 512–524.
15. Pawluk,A., Staals,R.H., Taylor,C., Watson,B.N., Saha,S., Fineran,P.C., Maxwell,K.L. and Davidson,A.R. (2016) Inactivation of CRISPR–Cas systems by anti-CRISPR proteins in diverse bacterial species. *Nat. Microbiol.*, **1**, 16085.
16. Marino,N.D., Zhang,J.Y., Borges,A.L., Sousa,A.A., Leon,L.M., Rauch,B.J., Walton,R.T., Berry,J.D., Joung,J.K., Kleinstiver,B.P. *et al.* (2018) Discovery of widespread type I and type V CRISPR–Cas inhibitors. *Science*, **362**, 240–242.
17. Pinilla-Redondo,R., Shehreen,S., Marino,N.D., Fagerlund,R.D., Brown,C.M., Sorensen,S.J., Fineran,P.C. and Bondy-Denomy,J.

(2020) Discovery of multiple anti-CRISPRs highlights anti-defense gene clustering in mobile genetic elements. *Nat. Commun.*, **11**, 5652.
18. Wang,J., Ma,J., Cheng,Z., Meng,X., You,L., Wang,M., Zhang,X. and Wang,Y. (2016) A CRISPR evolutionary arms race: structural insights into viral anti-CRISPR/Cas responses. *Cell Res.*, **26**, 1165–1168.
19. Wang,X., Yao,D., Xu,J.G., Li,A., Xu,J., Fu,P., Zhou,Y. and Zhu,Y. (2016) Structural basis of Cas3 inhibition by the bacteriophage protein AcrF3. *Nat. Struct. Mol. Biol.*, **23**, 868.
20. Zhang,K., Wang,S., Li,S., Zhu,Y., Pintilie,G.D., Mou,T.C., Schmid,M.F., Huang,Z. and Chiu,W. (2020) Inhibition mechanisms of AcrF9, AcrF8, and AcrF6 against type I-F CRISPR–Cas complex revealed by cryo-EM. *Proc. Natl. Acad. Sci. U.S.A.*, **117**, 7176–7182.
21. Hirschi,M., Lu,W.T., Santiago-Frangos,A., Wilkinson,R., Golden,S.M., Davidson,A.R., Lander,G.C. and Wiedenheft,B. (2020) AcrIF9 tethers non-sequence specific dsDNA to the CRISPR RNA-guided surveillance complex. *Nat. Commun.*, **11**, 2730.
22. Kim,I., Koo,J., An,S.Y., Hong,S.J., Ka,D., Kim,E.H., Bae,E. and Suh,J.Y. (2020) Structural and mechanistic insights into the CRISPR inhibition of AcrIF7. *Nucleic Acids Research*, **48**, 9959–9968.
23. Lu,W.T., Trost,C.N., Muller-Esparza,H., Randau,L. and Davidson,A.R. (2021) Anti-CRISPR AcrIF9 functions by inducing the CRISPR–Cas complex to bind DNA non-specifically. *Nucleic Acids Res.*, **49**, 3381–3393.
24. Wang,Q.S., Zhang,K.H., Cui,Y., Wang,Z.J., Pan,Q.Y., Liu,K., Sun,B., Zhou,H., Li,M.J. and Xu,Q. (2018) Upgrade of macromolecular crystallography beamline BL17U1 at SSRF. *Nuclear Sci. Tech.*, **29**, 68.
25. Zhang,W.Z., Tang,J.C., Wang,S.S., Wang,Z.J. and He,J.H. (2019) The protein complex crystallography beamline (BL19U1) at the Shanghai Synchrotron Radiation Facility. *Nuclear Science Techniques*, **30**, 170.
26. Otwinowski Z,M.W. (1997) Processing of X-ray diffraction data collected in oscillation mode. *Methods Enzymol.*, **276**, 307–326.
27. Adams,P.D., Grosse-Kunstleve,R.W., Hung,L.W., Ioerger,T.R., McCoy,A.J., Moriarty,N.W., Read,R.J., Sacchettini,J.C., Sauter,N.K. and Terwilliger,T.C. (2002) PHENIX: building new software for automated crystallographic structure determination. *Acta Crystallogr. D. Biol. Crystallogr.*, **58**, 1948–1954.
28. Emsley,P. and Cowtan,K. (2004) Coot: model-building tools for molecular graphics. *Acta Crystallogr. D. Biol. Crystallogr.*, **60**, 2126–2132.
29. Zheng,S.Q., Palovcak,E., Armache,J.P., Verba,K.A., Cheng,Y. and Agard,D.A. (2017) MotionCor2: anisotropic correction of beam-induced motion for improved cryo-electron microscopy. *Nat. Methods*, **14**, 331–332.
30. Zhang,K. (2016) Gctf: real-time CTF determination and correction. *J. Struct. Biol.*, **193**, 1–12.
31. Scheres,S.H. (2012) RELION: implementation of a Bayesian approach to cryo-EM structure determination. *J. Struct. Biol.*, **180**, 519–530.
32. Pettersen,E.F., Goddard,T.D., Huang,C.C., Couch,G.S., Greenblatt,D.M., Meng,E.C. and Ferrin,T.E. (2004) UCSF chimera – a visualization system for exploratory research and analysis. *J. Comput. Chem.*, **25**, 1605–1612.
33. Holm,L. (2020) DALI and the persistence of protein shape. *Protein Sci.*, **29**, 128–140.
34. Gabel,C., Li,Z., Zhang,H. and Chang,L. (2020) Structural basis for inhibition of the type I-F CRISPR–Cas surveillance complex by AcrIF4, AcrIF7 and AcrIF14. *Nucleic Acids Res.*, **49**, 584–594.
35. Szczelkun,M.D., Tikhomirova,M.S., Sinkunas,T., Gasiunas,G., Karvelis,T., Pschera,P., Siksnys,V. and Seidel,R. (2014) Direct observation of R-loop formation by single RNA-guided Cas9 and Cascade effector complexes. *Proc. Natl. Acad. Sci. U.S.A.*, **111**, 9798–9803.
36. Forsberg,K.J., Bhatt,I.V., Schmidtke,D.T., Javanmardi,K., Dillard,K.E., Stoddard,B.L., Finkelstein,I.J., Kaiser,B.K. and Malik,H.S. (2019) Functional metagenomics-guided discovery of potent Cas9 inhibitors in the human microbiome. *Elife*, **8**, e46540.
37. Rollins,M.F., Schuman,J.T., Paulus,K., Bukhari,H.S. and Wiedenheft,B. (2015) Mechanism of foreign DNA recognition by a CRISPR RNA-guided surveillance complex from Pseudomonas aeruginosa. *Nucleic Acids Res.*, **43**, 2216–2222.
38. Vink,J.N.A., Martens,K.J.A., Vlot,M., McKenzie,R.E., Almendros,C., Estrada Bonilla,B., Brocken,D.J.W., Hohlbein,J. and Brouns,S.J.J. (2020) Direct visualization of native CRISPR target search in live bacteria reveals cascade DNA surveillance mechanism. *Mol. Cell*, **77**, 39–50.